



A New Channel of Bulge Formation via the Destruction of Short Bars

Minghao Guo¹, Min Du², Luis C. Ho^{2,3}, Victor P. Debattista⁴, and Dongyao Zhao²¹Peking University, Beijing 100871, People's Republic of China²Kavli Institute for Astronomy and Astrophysics, Peking University, Beijing 100871, People's Republic of China; dumin@pku.edu.cn³Department of Astronomy, School of Physics, Peking University, Beijing 100871, People's Republic of China⁴Jeremiah Horrocks Institute, University of Central Lancashire, Preston PR1 2HE, UK

Received 2019 August 30; revised 2019 November 3; accepted 2019 November 15; published 2020 January 8

Abstract

Short (inner) bars of subkiloparsec radius have been hypothesized to be an important mechanism for driving gas inflows to small scales, thus feeding central black holes (BHs). Recent numerical simulations have shown that the growth of central BHs in galaxies can destroy short bars, when the BH reaches a mass of $\sim 0.1\%$ of the total stellar mass of the galaxy. We study N -body simulations of galaxies with single and double bars to track the long-term evolution of the central stellar mass distribution. We find that the destruction of the short bar contributes significantly to the growth of the bulge. The final bulge mass is roughly equal to the sum of the masses of the initial pseudo bulge and short bar. The initially boxy/peanut-shaped bulge of Sérsic index $n \lesssim 1$ is transformed into a more massive, compact structure that bears many similarities to a classical bulge, in terms of its morphology ($n \approx 2$), kinematics (dispersion-dominated, isotropic), and location on standard scaling relations (Kormendy relation, mass-size relation, and correlations between BH mass and bulge stellar mass and velocity dispersion). Our proposed channel for forming classical bulges relies solely on the destruction of short bars without any reliance on mergers. We suggest that some of the less massive, less compact classical bulges were formed in this manner.

Unified Astronomy Thesaurus concepts: [Galaxy dynamics \(591\)](#); [Galaxy physics \(612\)](#); [Galaxy bulges \(578\)](#); [Black hole physics \(159\)](#); [Galaxy structure \(622\)](#); [Galaxy evolution \(1052\)](#)

1. Introduction

Galaxies are generally considered as composite stellar systems comprising a fast-rotating disk and a more slowly rotating bulge. How bulges form is an important topic in understanding the evolution of galaxies. Bulges come in two flavors. From a purely morphological perspective, classical bulges are highly concentrated, featureless spheroids, while pseudo bulges, characteristically hosted by late-type galaxies, are a more flattened, lower surface density component that often coexists with complex central substructures such as nuclear bars, disks, rings, and spirals (Kormendy & Kennicutt 2004). Pseudo and classical bulges are thought to have completely different formation mechanisms. It is plausible that classical bulges are the end products of major mergers of gas-rich galaxies. Tidal torques drive efficient gas inflows during gas-rich mergers, which lead to rapid central (kiloparsec-scale) starbursts and bulge build-up (e.g., Hernquist 1989; Barnes & Hernquist 1996; Hopkins et al. 2009). Other processes, besides mergers, may also contribute to the growth of classical bulges. Zoom-in cosmological simulations suggest that misaligned accretion of gas can form bulges by in situ starbursts, placing less emphasis on the role of mergers (Scannapieco et al. 2009; Sales et al. 2012; Zolotov et al. 2015). Gas-rich disks at high redshifts are gravitationally unstable to the formation of massive clumps, mergers of which provide yet another avenue to concentrate stars in the central regions of galaxies (Vandenbergh et al. 1996; Noguchi 1998, 1999; Elmegreen & Elmegreen 2005; Bournaud et al. 2008; Genzel et al. 2008; Dekel et al. 2009; Clarke et al. 2019). Elmegreen et al. (2008) suggest that the clumps coalesce into a “classical” bulge. By contrast, Inoue & Saitoh (2012) and Du et al. (2015) argue that such clumps manufacture pseudo bulges/bars with significant rotation, bar-like morphology, and an exponential surface density profile. Even massive classical bulges can have diverse

merger histories (Bell et al. 2017). Park et al. (2019) suggest that roughly half of the spheroidal component in disk-dominated galaxies arises from orbits aligned with the disk; such disk stars continuously migrate to the center, without the aid of perturbations from mergers. Wang et al. (2019) similarly emphasized the contribution of disk star migration to bulge growth.

Pseudo bulges are thought to form through secular evolution of the large-scale disks of spiral galaxies, with bars being a key agent of angular momentum redistribution. Bars can funnel gas efficiently into the central regions of galaxies by bar-driven shocks, forming nuclear rings (e.g., Athanassoula 1992; Kim et al. 2012; Li et al. 2015), disks, or bars (Shlosman et al. 1989). Nuclear disks are likely to be classified as pseudo bulges morphologically. On the other hand, although boxy/peanut bulges are also classified as pseudo bulges, while they are likely to be a part of bars that buckle vertically (e.g., Raha et al. 1991). Additionally, some cosmological simulations (e.g., Okamoto 2013) suggest that pseudo bulges can form from the rapid supply of low angular momentum gas at $z \gtrsim 2$, before the assembly of disks. In this case, pseudo bulges can be older than those forming in the secular evolution of disks ($z \lesssim 1$).

The empirical correlations between central black hole (BH) mass and bulge properties (Ferrarese & Merritt 2000; Gebhardt et al. 2000; Tremaine et al. 2002; Häring & Rix 2004; Gültekin et al. 2009) have prompted numerous suggestions that the two coevolve in some manner. However, as reviewed by Kormendy & Ho (2013), the correlations are tight only for classical bulges and elliptical galaxies. Pseudo bulges exhibit a markedly larger scatter and lower zero-point, and it is unclear what effect, if any, BHs have on their evolution. Indeed, the least massive central BHs known, with mass $M_{\text{BH}} \approx 10^4 - 10^6 M_{\odot}$, live in essentially bulgeless galaxies (Filippenko & Ho 2003; Barth et al. 2004; Greene et al. 2008; Jiang et al. 2011; see

Greene et al. 2019 for a review, 2019, in preparation). BHs evidently do not require bulges to form (Ho 2008). Further, the mere existence of disk-dominated active galaxies (e.g., Cisternas et al. 2011; Kim et al. 2017; Zhao et al. 2019) implies that BHs can grow by internal secular processes alone.

Stellar bars can drive gas to subkiloparsec-scale efficiently, but transporting gas to yet smaller radii becomes challenging without the aid of smaller scale nonaxisymmetric structures (Hopkins & Quataert 2010), such as a short inner bar in double-barred (S2B) galaxies (Shlosman et al. 1989). Roughly one-third of barred galaxies in the local universe are observed to be S2B galaxies (Erwin & Sparke 2002; Laine et al. 2002; Erwin 2004). Debattista & Shen (2007) for the first time successfully generated a long-lived S2B structure in N -body simulations. The systematic study of Du et al. (2015) demonstrated that a short (inner) bar can form spontaneously without involving gas from an initially dynamically cool, nuclear stellar disk due to its own bar instability (see also Wu et al. 2016). The addition of gas was considered by Wozniak (2015).

The inner short bar promotes the accretion onto the central BH, but the BH, in turn, mediates its own growth by destroying the bar (Du et al. 2017). The destruction of bars under the dynamical influence of central massive concentrations (e.g., BHs) has long been studied (e.g., Gerhard & Binney 1985; Hasan & Norman 1990; Pfenniger & Norman 1990). It is well known that an unrealistically massive BH ($>4\%$ of total stellar mass M_*) is needed to destroy a large-scale bar (Shen & Sellwood 2004; Athanassoula et al. 2005a; Debattista et al. 2006). Hozumi (2012) suggested that a weaker bar is not as robust as a large-scale bar. Du et al. (2017) found a BH of mass $M_{\text{BH}} \approx 10^{-3} M_*$ destroys a short bar of 1 kpc scale quickly and hence suppresses its own growth. Thus, the maximum mass of BHs allowed in the secular evolution is about $10^{-3} M_*$, which is consistent with observations (e.g., Kormendy & Ho 2013; Reines & Volonteri 2015). In this paper, we define “short bars” as bars of radius $\lesssim 1.5$ kpc scale, no matter whether they coexist with an outer bar. Thus, short bars can be the inner bar of S2B galaxies or small-size bar of single-barred galaxies.

What is the remnant of the destroyed short bar? We expect the dissolved bar to become a denser, more axisymmetric structure. Can it be identified observationally? How does it affect the properties of bulges? Following on the work of Du et al. (2017), we here investigate in detail the properties of the remnant short bar. Section 2 describes our simulations. The process of morphological decomposition is presented in Section 3. The results of the decomposition and the intrinsic properties of the bulges are shown in Section 4. A physical scenario for the secular coevolution of BHs and bulges is discussed in Section 5. We summarize our conclusions in Section 6.

2. Simulations

2.1. Setup

We use the method first presented by Du et al. (2015) to generate galaxies with short bars: dynamically cold, rotation-dominated inner/nuclear disks are introduced in the central regions of pure-disk models. The simulations are run with the three-dimensional cylindrical polar grid option of the GALAXY N -body code (Sellwood 2014), which increases the force resolution toward the center. The units system of the simulations is

Table 1
Basic Properties of the Models

Model ^a	$b_{Q_{\min}}$ ^b	$M_{\text{BH,max}} (M_*)$	$R_{\text{bar}}(\text{kpc})^c$	Type ^d
S2B_a	0.5	2×10^{-3}	0.9 7.0	S2B
SB_a	0.7	2×10^{-3}	1.5 ...	SB
SB_b	0.9	2×10^{-3}	... 6.3	SB
S2B_a0	0.5	10^{-4}	0.9 7.0	S2B
SB_a0	0.7	10^{-4}	1.5 ...	SB
SB_b0	0.9	10^{-4}	... 6.3	SB

Notes.

^a Name of the models. S2B_a0, SB_a0, and SB_b0 are the control models of S2B_a, SB_a, and SB_b, respectively. The only difference between each pair is the maximum mass of BHs $M_{\text{BH,max}}$. In the control models, the BHs have little effect on the bar evolution.

^b The minimum value of Toomre Q at the center, quantifying the dynamical temperature of initial inner disk.

^c Half-size radius of inner/short-scale (left column) and outer/large-scale (right column) bar measured by the minimum radius obtained from tracing half-way down the peak of the $m = 2$ amplitude (Figure 2) and the 10° deviation from a constant phase angle at $t = 2.8$ Gyr in models S2B_a(0), SB_a(0), and SB_b(0), when the BH has no significant effect.

^d S2B: double-barred galaxy; SB: single-barred galaxy. Note that in SB_a a weak, longer bar forms after the BH destroys the short bar.

$G = M_0 = h_R = T_0 = V_0 = 1$, where G , M_0 , h_R , T_0 , and V_0 are the units of the gravitational constant, mass, length, time, and velocity, respectively. We scale the models to mimic typical spiral galaxies by setting $M_0 = 4 \times 10^{10} M_\odot$ and the initial scale length of the purely exponential disk to $h_R = 2.5$ kpc, which gives $T_0 = \sqrt{h_R^3/GM_0} \approx 9.3$ Myr and $V_0 = \sqrt{GM_0/h_R} \approx 262$ km s⁻¹. This scaling is the same as that used in Du et al. (2015). The simulation box measures $N_R \times N_\phi \times N_z = 58 \times 64 \times 375$, which gives a force resolution of ~ 25 pc in the central regions. Such a grid can sufficiently resolve the dynamics of 1 kpc-scale short bars (Du et al. 2015).

The basic properties of the models are given in Table 1. All of the models are initially composed of a live disk, a rigid dark matter halo, and a tiny BH. To simplify the simulations, we use rigid potentials to mimic dark matter halos, as the central dynamics are largely dominated by the stellar component. The halo potential is logarithmic, $\Phi(r) = 0.5V_h^2 \ln(r^2 + r_h^2)$, where $V_h = 0.6V_0$ and $r_h = 15h_R$. The purely exponential disk of mass $M_* = 1.5M_0$ and initial scale length h_R consists of four million equal-mass particles. Their gravitational force is softened with a radius of $0.01h_R = 25$ pc. We use an additional potential of Plummer form, $\Phi_{\text{BH}}(r) = -GM_{\text{BH}}(t)/\sqrt{r^2 + \epsilon_{\text{BH}}^2}$, where $\epsilon_{\text{BH}} = 0.01h_R = 2.5$ pc, to represent the central BH. The BH mass, M_{BH} , is the same as the stellar particles before $t = 300T_0 = 2.8$ Gyr, thus having no effect on the overall evolution of the models. Then it grows smoothly and adiabatically over 50 time units (~ 0.5 Gyr) from the level of stellar particles to a maximum value $M_{\text{BH,max}}$, following a cosine function (see details in Du et al. 2017). $M_{\text{BH,max}}$ used in each model is given in the third column of Table 1. At later times, M_{BH} is kept constant at $M_{\text{BH,max}}$. It is worth mentioning that the force from the BH is added to each particle from the analytic form, and is therefore independent of the grid resolution. The guard shell technique is employed to reduce the time steps of gravitational integration around the BH (see details in Shen & Sellwood 2004; Du et al. 2017).

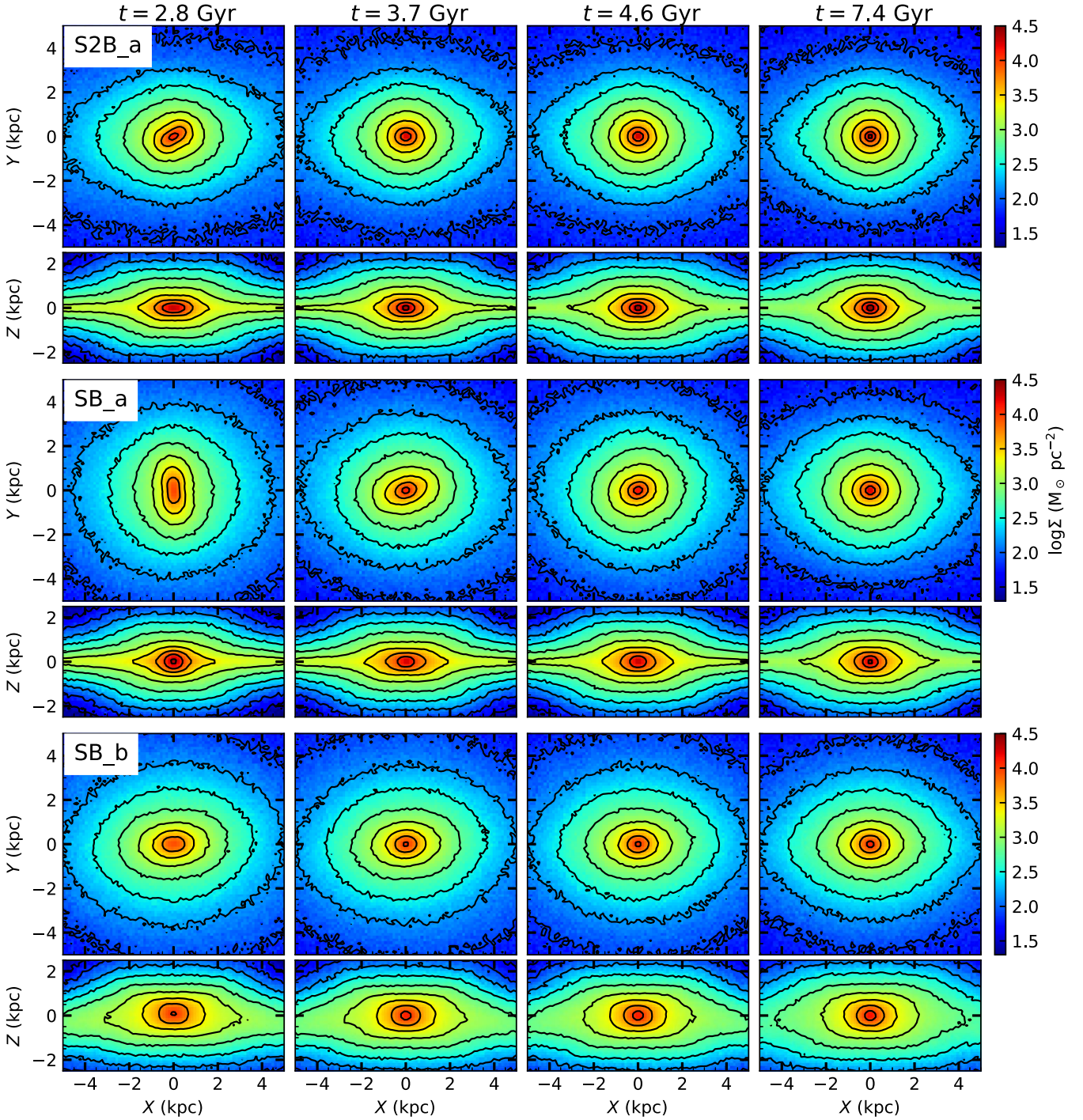


Figure 1. Face-on (upper panels) and edge-on (lower panels) surface density distributions of models S2B_a, SB_a, and SB_b (from top to bottom). From left to right, we show the cases at times $t = 2.8, 3.7, 4.6,$ and 7.4 Gyr, respectively. All the images are presented using the same color bar and contours. The outer bars are aligned with the x -axis. These images clearly show that the short bars of models S2B_a and SB_a are destroyed by the BH, forming a spheroidal, denser structure in the central region.

The models are named S2B_a(0), SB_a(0), and SB_b(0), according to their bar structures (see Figure 1 for the face-on and edge-on surface density distributions). The nomenclature S2B_a(0) represents both S2B_a and S2B_a0, and likewise for SB_a(0) and SB_b(0). S2B_a(0) has a double-barred structure. Du et al. (2016) studied the kinematic properties of model S2B_a0 and concluded that they are consistent with observed S2Bs. Thus, S2B_a(0) was used as the standard model of S2Bs in Du et al. (2015, 2016, 2017). In this paper, we include new

models SB_a(0) and SB_b(0) that have exactly the same halo and BH as S2B_a(0). Their main difference is in their bars. Both SB_a(0) and SB_b(0) have only a single bar, while the bar in SB_a(0) of radius ~ 1.5 kpc is much shorter than that of SB_b(0); it is, in other words, a short bar (see bar size, R_{bar} , in Table 1). We approximate the bar size—marked by vertical lines in Figure 2—as the minimum radius obtained by tracing half of the amplitude of the peak of the $m = 2$ Fourier component (A_2/A_0) and the 10° deviation from a constant ϕ at

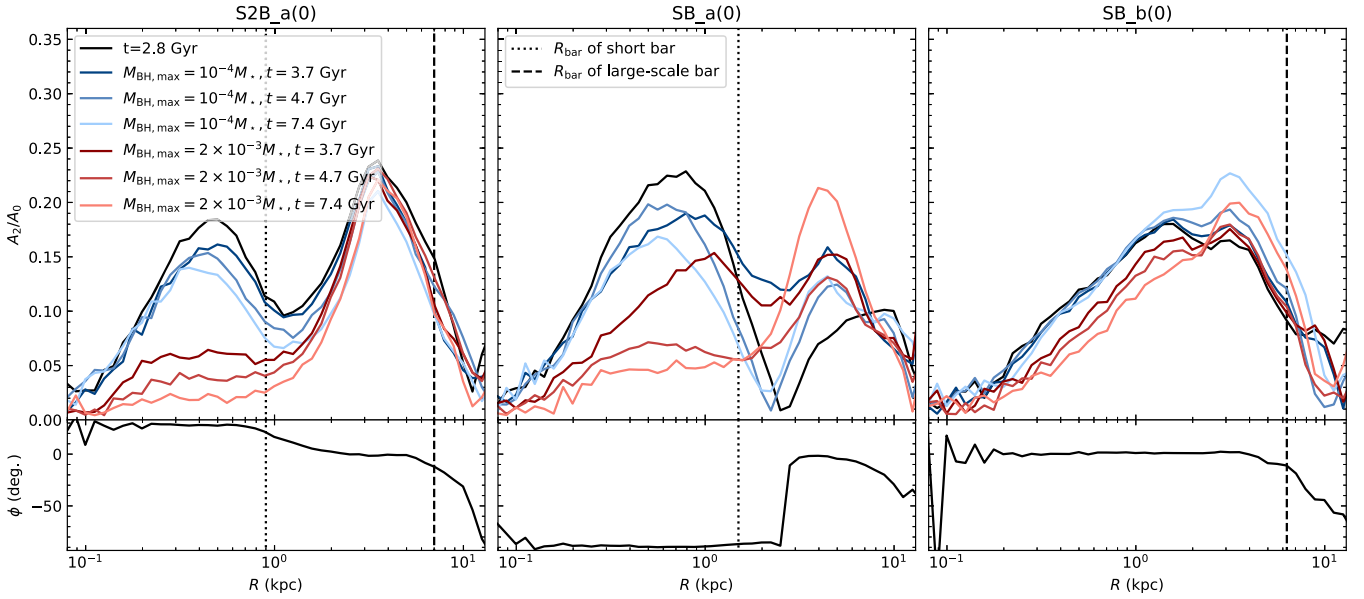


Figure 2. Time evolution of A_2/A_0 in models S2B_a(0), SB_a(0) and SB_b(0) (from left to right), where A_2 and A_0 are the Fourier $m = 2$ and $m = 0$ modes, respectively, measured in annuli of equal radial interval in logarithmic space. The red and blue profiles correspond to the models of BH mass $M_{\text{BH,max}} = 2 \times 10^{-3} M_\star$ and $10^{-4} M_\star$, respectively, at $t \geq 3.7$ Gyr. The black profile in each panel is the case of $t = 2.8$ Gyr. The bottom panels show the phase angle ϕ of the bars at $t = 2.8$ Gyr. The sizes of short/inner and large-scale/outer bars are marked by the dotted and dashed vertical lines, respectively.

$t = 2.8$ Gyr. Note that, in SB_a(0) at $t = 2.8$ Gyr, the weak $m = 2$ component having $A_2/A_0 \approx 0.1$ and ellipticity $\epsilon \approx 0.15$ at $r \approx 7$ kpc is not strong enough to be considered as an outer bar.

The formation of bars is largely determined by Toomre’s (1964) Q parameter of the disk. We set $Q \approx 2$ in the outer part of the disk; in the inner part ($R \lesssim 4.4$ kpc), Q is reduced gradually toward the center. This results in a dynamically cool inner disk, reaching a minimum value b_Q at the center. Thus, we use b_Q (Table 1) to represent the dynamical temperature of the inner disk. The dynamically cool inner disk leads to the formation of the inner bar in model S2B_a(0) and the short bar in model SB_a(0) (see more in Du et al. 2015). In the following section, we present the evolution of these models under the dynamical influence of the BH. This work only considers the dynamical effect of the BH; no hydrodynamic processes are included.

2.2. Evolution: the Destruction of Short Bars Due to the Growth of BHs

Figures 1 and 2 show the evolution of models S2B_a(0), SB_a(0), and SB_b(0). At $t \leq 2.8$ Gyr, models S2B_a0, SB_a0, and SB_b0 are identical to S2B_a, SB_a, and SB_b, respectively. The BH masses of the main group (S2B_a, SB_a, SB_b) increase to $M_{\text{BH,max}} = 2 \times 10^{-3} M_\star$, reaching a typical observed BH mass fraction. For comparison, the BH is unimportant ($M_{\text{BH,max}} = 10^{-4} M_\star$) over the entire simulation of the control group (S2B_a0, SB_a0, SB_b0).

The evolution of the models can be separated into three phases:

- (1) Bars and boxy/peanut-shaped bulges form spontaneously. At $t \leq 2.8$ Gyr, all of the models form bars and boxy/peanut bulges spontaneously due to their internal dynamical instabilities (the first column of Figure 1). All bars have reached steady state. At this stage the BH is still small and has no significant effect on

the evolution of their hosts. As shown in the edge-on images in Figure 1, boxy/peanut bulges form due to the buckling instability triggered by bars, probably large-scale bars.

- (2) Short (inner) bars are destroyed due to the growth of the BH. At $2.8 < t \leq 3.3$ Gyr, the BH grows smoothly to the maximum mass $M_{\text{BH,max}}$. The short bars of S2B_a and SB_a are completely destroyed by the BH, in about 0.4 Gyr and 1.4 Gyr (the second and third columns of Figure 1), respectively. A spheroidal component forms in the central region, where A_2/A_0 decreases significantly (the series of red profiles in Figure 2). Using $M_{\text{BH,max}} = 10^{-4} M_\star$ produces a minor effect in models S2B_a0 and SB_a0, with the short bars surviving until the end of the simulations (the series of blue profiles). In SB_b, the central region of the bar becomes rounder, but this effect is not as pronounced as in both S2B_a and SB_a.
- (3) Steady phase. After the short bars are destroyed, the galaxies evolve slowly. The morphology is unchanged until the end of the simulation.

In order to study the properties of the remnant of the short bar destruction, we decompose the models in Section 3. The changes in morphology are investigated from an observational point of view.

3. Morphological Decomposition

3.1. Setup for GALFIT

We employ the latest version of GALFIT (Peng et al. 2002, 2010)—a widely used standard tool for decomposing galaxy images—to investigate the morphological structures of the models. We generate mock observational images using a Cartesian grid covering a region of 30×30 kpc². Each cell has an equal size of 0.1×0.1 kpc² that is sufficient for decomposing all structures. To test the effect of inclination, we project all of the models to typical inclination angles of $i = 0^\circ$ (i.e.,

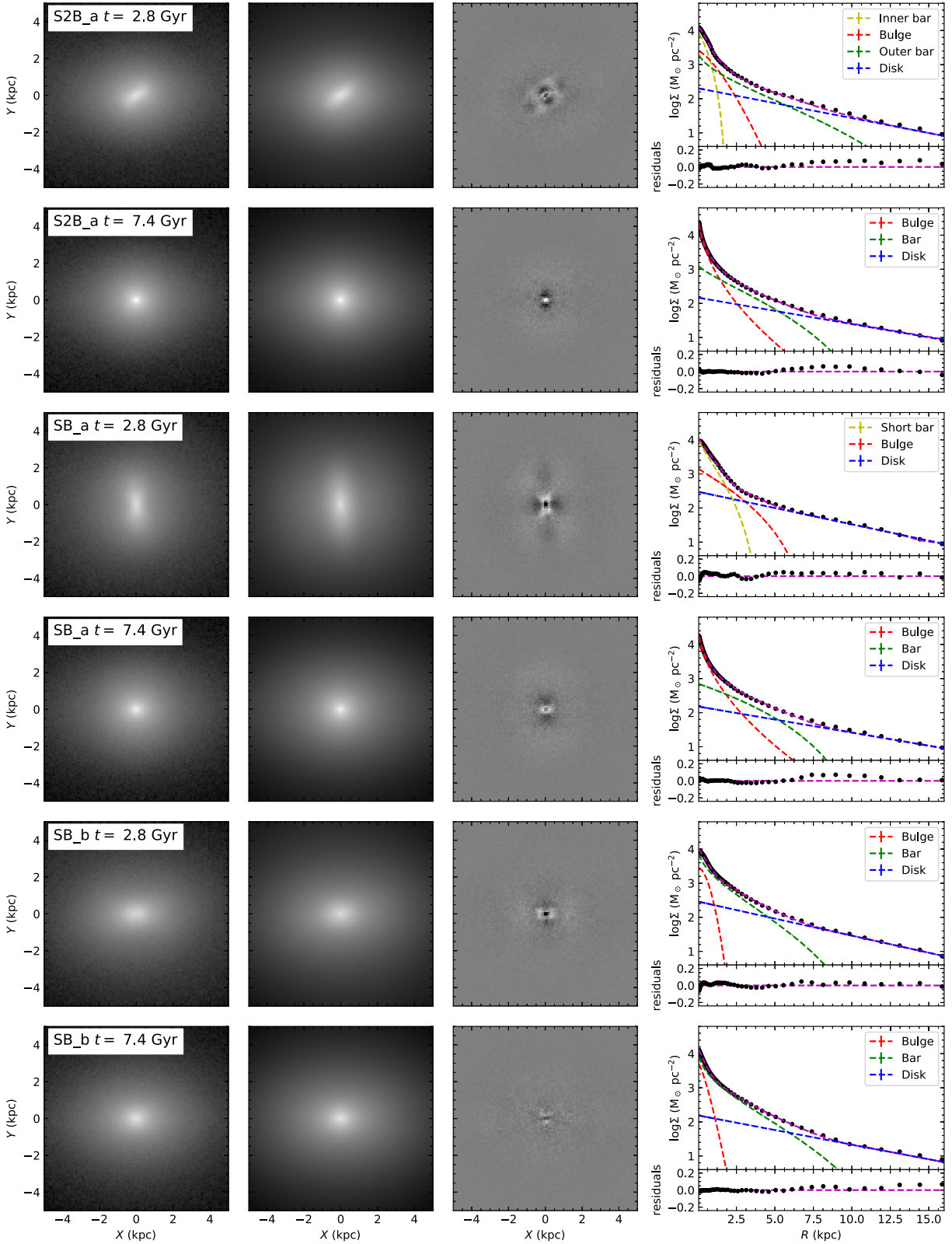


Figure 3. Morphological decomposition using GALFIT. From top to bottom, we show the three models at $t = 2.8$ Gyr and $t = 7.4$ Gyr, which correspond, respectively, to the time when the BH starts to grow and the final time of each simulation. From left to right, we show images of the models, the GALFIT fitting, the residuals, and the 1D profiles, respectively. The field of view is 10×10 kpc². The images are shown using the same logarithmic stretch for the model and fitting image, and histogram equalization stretch is used for the residual image. In the right panels, we show the 1D density profiles of each component used in the GALFIT model. The magenta lines correspond to the overall density profiles of the GALFIT fit. The residuals are shown in the lower part of the right panels. Both the bulges and bars are described by Sérsic profiles; modeling the bar with a Ferrers function gives similar results.

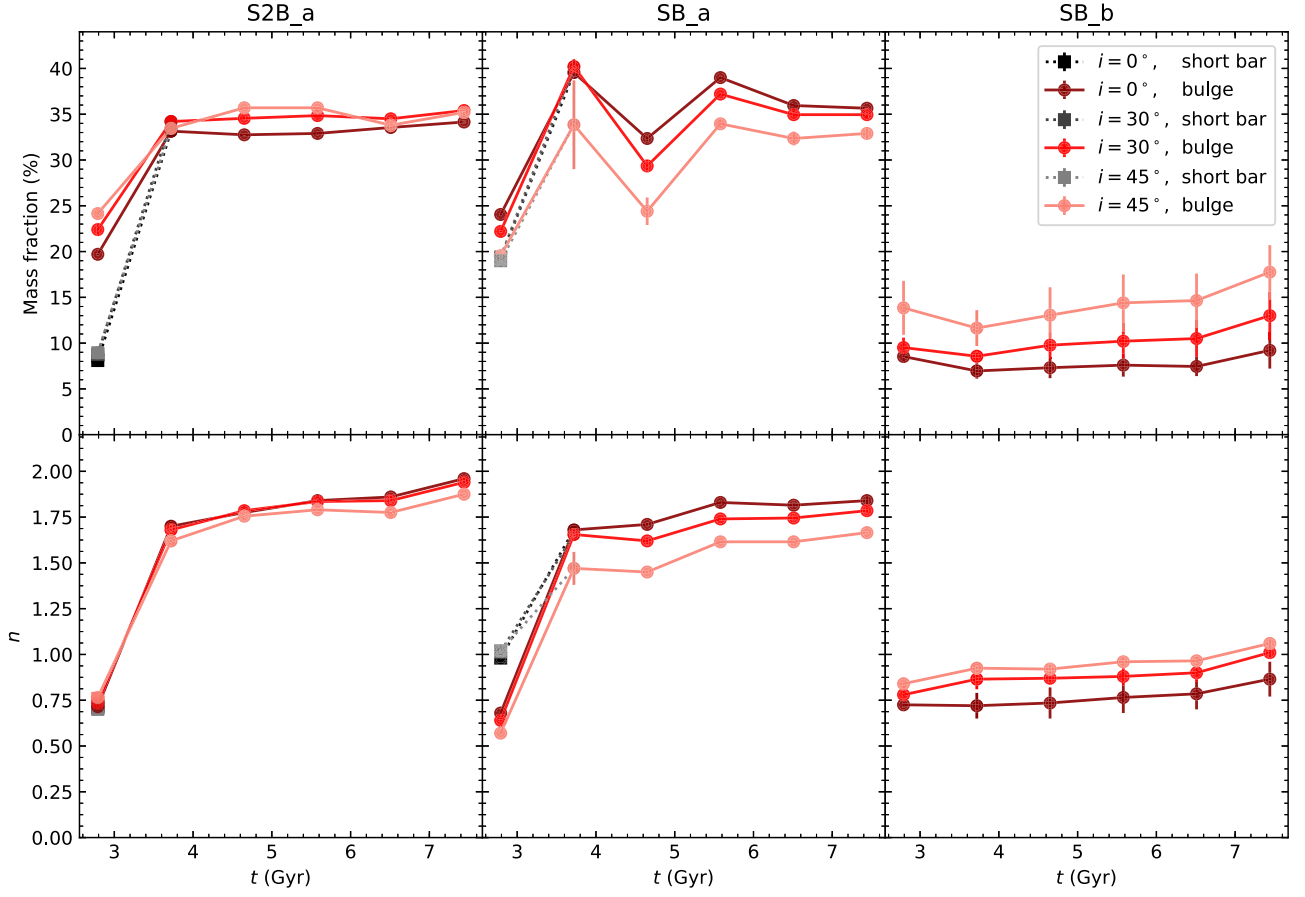


Figure 4. Evolution of the mass fraction (top) and Sérsic index n (bottom) of the bulges in S2B_a, SB_a, and SB_b (from left to right). The results of the short bars are overlaid for models S2B_a and SB_a. The error bars represent the results obtained using Ferrers and Sérsic bars; the dots mark their average values. The error bars are generally smaller than the size of the symbols, except for the case of $i = 45^\circ$. The squares show the mass fraction and Sérsic index of the short bars. From dark to light colors, we vary the inclination angle from $i = 0^\circ$ to 45° .

face-on, Figure 3), 30° , and 45° . We do not account for the effects of sky background or point-spread function.

All of the models are centered at the coordinate origin. The azimuthal shape of each component is the pure ellipse

$$r(x, y) = \sqrt{x^2 + \left(\frac{y}{1 - \epsilon}\right)^2}, \quad (1)$$

where ϵ is the ellipticity. We use a simple exponential profile to fit the disk component,

$$\Sigma(r) = \Sigma_0 \exp\left(-\frac{r}{r_s}\right), \quad (2)$$

where r_s is the scale length and Σ_0 is the central surface density. Bulges are described by the Sérsic function

$$\Sigma(r) = \Sigma_e \exp\left[-\kappa \left(\left(\frac{r}{r_e}\right)^{1/n} - 1\right)\right], \quad (3)$$

where r_e is the half-mass (effective) radius, and Σ_e is the surface density at r_e . The Sérsic index n is generally used to represent the concentration, and κ satisfies $\Gamma(2n) = 2\gamma(2n, \kappa)$, where Γ and γ are the gamma function and incomplete gamma function, respectively.

The bar is fit using both the Sérsic function and the modified Ferrers function, which is given as

$$\Sigma(r) = \Sigma_0(1 - (r/r_{\text{out}})^{2-\beta})^\alpha, \quad (4)$$

where r_{out} is the radius of the outer truncation, Σ_0 is the central surface density, and α and β control the sharpness of the outer truncation and the central concentration, respectively.

3.2. Decomposition of Individual Models

Figure 3 shows the morphological decomposition of the face-on images of models S2B_a, SB_a, and SB_b. The columns show, respectively, the logarithmic surface densities of the models, the fitting results obtained by GALFIT, and the residuals. The BH is tiny at $t = 2.8$ Gyr, the starting point of Phase 2. The snapshots at $t = 7.4$ Gyr represent the morphological decomposition after the short bars have been destroyed. During the steady phase (Phase 3), the morphologies of all models show little variation. It is clear from the one-dimensional (1D) radial density profiles of the individual components (fourth column) that all models are well fitted (residuals < 0.05). Each model includes an exponential disk, a bulge, and one or two bar components. The bulge components possibly correspond to the boxy/peanut-shaped bulges that are clearly seen in the edge-on plots of Figure 1. Two bars are required in order to fit S2B_a(0) at $t = 2.8$ Gyr (Figure 3); after the short bar is destroyed, only one bar is used (e.g., the cases at

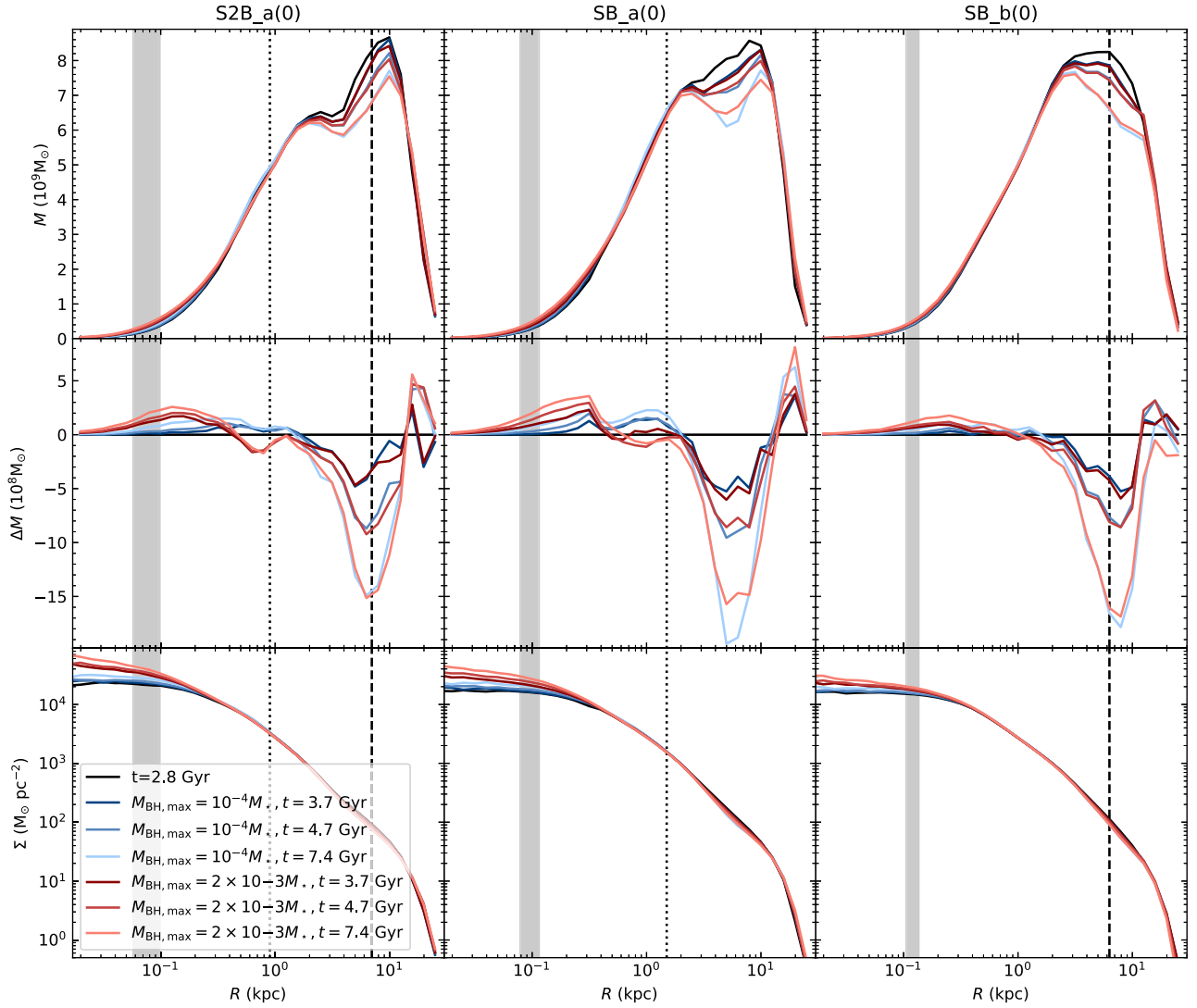


Figure 5. Top: mass distribution per logarithmic bin of radius R . Middle: the difference of mass distribution between $t = 2.8$ Gyr and the other time steps. Bottom: surface density profiles. From left to right, the three models [S2B_a(0), SB_a(0), and SB_b(0)] are shown. The red and blue series of profiles represent models with BHs of $M_{\text{BH,max}} = 2 \times 10^{-3} M_*$ and $M_{\text{BH,max}} = 10^{-4} M_*$, respectively. The gray region shows the range of the sphere-of-influence of the BH, within which the stellar mass is equal to the BH mass. The sizes of short/inner bars and large-scale/outer bars are marked by dotted and dashed vertical lines.

$t = 7.4$ Gyr). The single-barred models SB_a(0) and SB_b(0) always include one bar component. Note that in SB_a a weak, longer bar forms after its short bar is destroyed. In comparison, SB_a0 only has a single short bar, as the ellipticity of its outer disk is always < 0.2 . The peak at $R \approx 4$ kpc (small peak of Figure 2) corresponds to the newly formed outer bar in SB_a. The value of A_2/A_0 increases from 0.15 to 0.21 during 3.7–7.4 Gyr, perhaps due to the destruction of the short bar.

4. Results

This section shows the results of the morphological decomposition. We investigate the evolution of the bulges, not only in terms of morphology, but also the intrinsic exchange of mass and angular momentum.

4.1. The Growth of Bulges after Short Bar Destruction

Figure 4 illustrates the evolution of the mass fraction and Sérsic index of the bulges in S2B_a, SB_a, and SB_b. The effect of inclination angle is tested in the range $i = 0^\circ$ – 45° . We

use the upper and lower limits of the error bars to represent the results obtained by using Ferrers and Sérsic bars, respectively; the dot symbols mark their average values. Ferrers function generally gives more massive bars than the Sérsic function, as a result of which the bulge mass is slightly larger when a Sérsic bar is used. For models S2B_a and SB_a, we overlay the properties of their short bars at $t = 2.8$ Gyr (square symbols), after which the short bars are destroyed quickly. The dotted lines indicate a potential evolution track by which the remnants of short bars contribute to the growth of bulges. In comparison, the bulge properties of the control group evolve mildly during $t > 2.8$ Gyr (not shown here).

The bulge masses of S2B_a and SB_a clearly increase significantly after their short bars are destroyed. The inner bar of S2B_a ($R_{\text{bar}} \approx 0.9$ kpc, mass $\sim 0.08 M_*$) is destroyed in ~ 0.4 Gyr during Phase 2 (Section 2), while for model SB_a it takes ~ 1.4 Gyr to destroy the short bar, which is longer ($R_{\text{bar}} \approx 1.5$ kpc) and more massive ($\sim 0.2 M_*$). Although the two short bars differ greatly in strength, they evolve similarly: a massive ($\sim 0.35 M_*$), centrally concentrated (Sérsic index

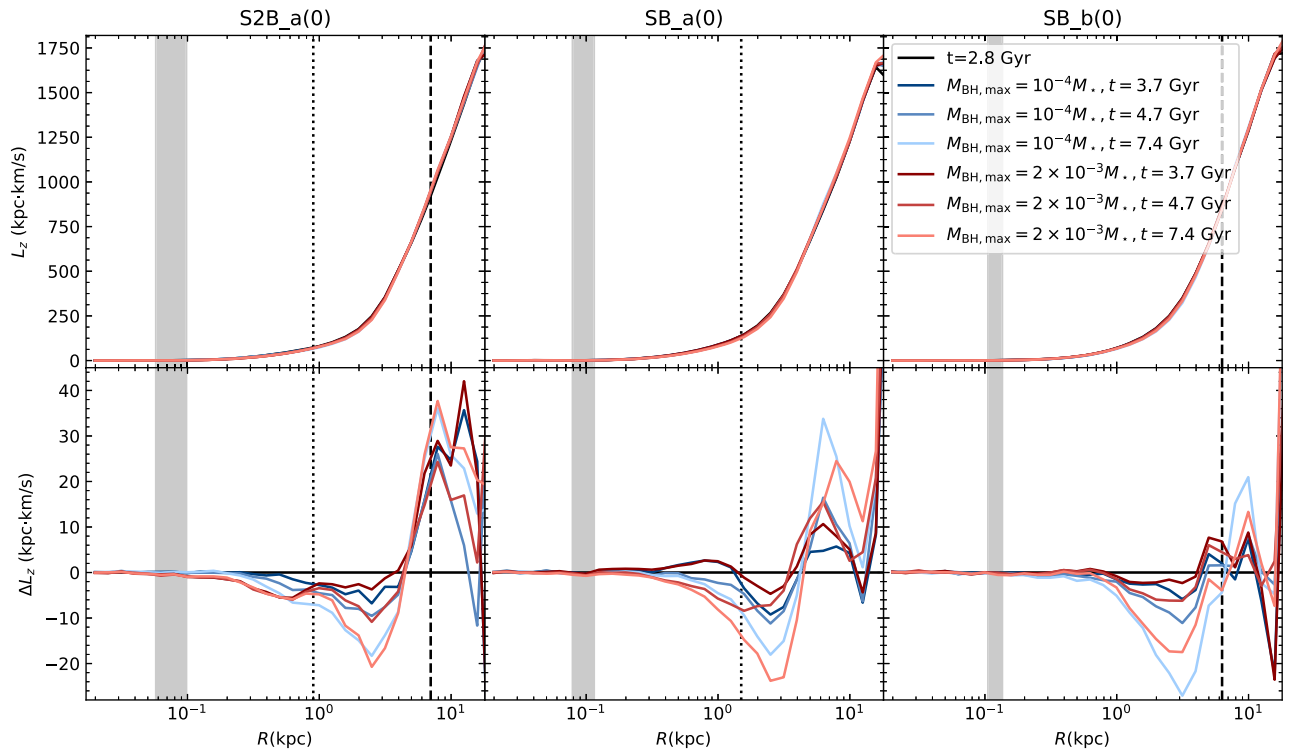


Figure 6. Similar to Figure 5, the distribution of specific angular momentum (L_z ; top) per logarithmic bin of radius and the difference between $t = 2.8$ Gyr and the other time steps (ΔL_z ; bottom). The red and blue series of profiles represent the models with BHs of $M_{\text{BH,max}} = 2 \times 10^{-3} M_*$ and $M_{\text{BH,max}} = 10^{-4} M_*$, respectively.

$n \approx 1.75$) bulge forms in the aftermath of the destruction of the short bar. As a consequence, the formerly boxy/peanut-shaped bulge (with $n < 1$) takes on more of an appearance of a classical bulge. The Sérsic index increased to a value close to 2 without involving any external perturbation. A Sérsic index of $n \gtrsim 2$ is generally used as a criterion for defining classical bulges (Fisher & Drory 2008; but see Gao et al. 2019b). For comparison, the bulge of the single-barred case (SB_b; right panels) has changed little. This is consistent with the numerical simulations of Debattista et al. (2004) showing that box/peanut bulges are able to maintain a low Sérsic index ($n < 1.5$). All of the results above are roughly independent of inclination angle and choice of bar function. After $t = 4$ Gyr (Phase 3), all the bulges evolve slowly.

The particles of the destroyed short bars become incorporated as part of the bulges. The bulge masses of both S2B_a and SB_a are similar to the sum of the masses of their short bars and progenitor bulges. There are residual differences at the level of $\sim 0.1 M_*$, which may reflect inward mass transport or the uncertainty of the morphological decomposition. About half of the mass of the resultant bulges is from the progenitor bulges. The properties of resultant bulges are largely determined by both the progenitor bulges and the relics of the short bars.

4.2. Redistribution of Mass and Angular Momentum

To understand the growth of the bulges, we investigate the transport of mass ($M(t)$; Figure 5) and angular momentum ($L_z(t)$; Figure 6) during $t = 2.8$ –7.4 Gyr. The profiles of $M(t)$ and $L_z(t)$ (first row) and their differentials between different epochs (ΔM and ΔL_z ; second row) are measured in annuli of equal radial interval in logarithmic space. Figure 5 further

shows the evolution of the radial surface density profile, which is pronounced within the BH's sphere-of-influence.

The effect of the destruction of the short bar can be seen clearly by comparing the destruction of models with $M_{\text{BH,max}} = 2 \times 10^{-3} M_*$ (red profiles) with the control group with $M_{\text{BH,max}} = 10^{-4} M_*$ (blue profiles). Consistent with Athanassoula (2005a) and Debattista et al. (2006), stars are transported outward by gaining angular momentum around the corotation radius of the outer bar. Thus, the regions of $\Delta M < 0$ and the turning point of ΔL_z are roughly consistent with the outer ends of the bar (marked by vertical dashed lines). This mechanism is efficient even in the case of the extremely weak bar at $R \approx 5$ kpc for SB_a(0), and the behavior is very similar for both the main and the control groups. We confirmed that the outer bars are fast bars, based on the criterion of Debattista et al. (2002). There is no clear signature of outward mass transfer around the ends of the short bars, possibly because the short bars, being slow, are much shorter than their corotation radii (~ 3.5 kpc; Du et al. 2015), rendering angular momentum exchange inefficient. In the control group, the mild increase of mass ($\Delta M > 0$) in the central region might be partially due to long-term asymmetric drift or the inward migration of stars that lose angular momentum around the outer bar's corotation radius. Models S2B_a and SB_a ($M_{\text{BH,max}} = 2 \times 10^{-3} M_*$) apparently transfers more mass from ~ 1 kpc to < 300 pc due to the destruction of the short bar during 2.8–3.7 Gyr (Phase 2). As a consequence, the central surface density (the third row of Figure 5) becomes cuspier. However, the additional mass transport is only about 1%–2% of M_* . The red series of ΔL_z profiles have smaller values at $R < 1$ kpc, suggesting that angular momentum is transferred outward as a result of short bar destruction, although this effect is not significant. After $t = 3.7$ Gyr, the changes in mass and angular momentum are minor at the central regions.

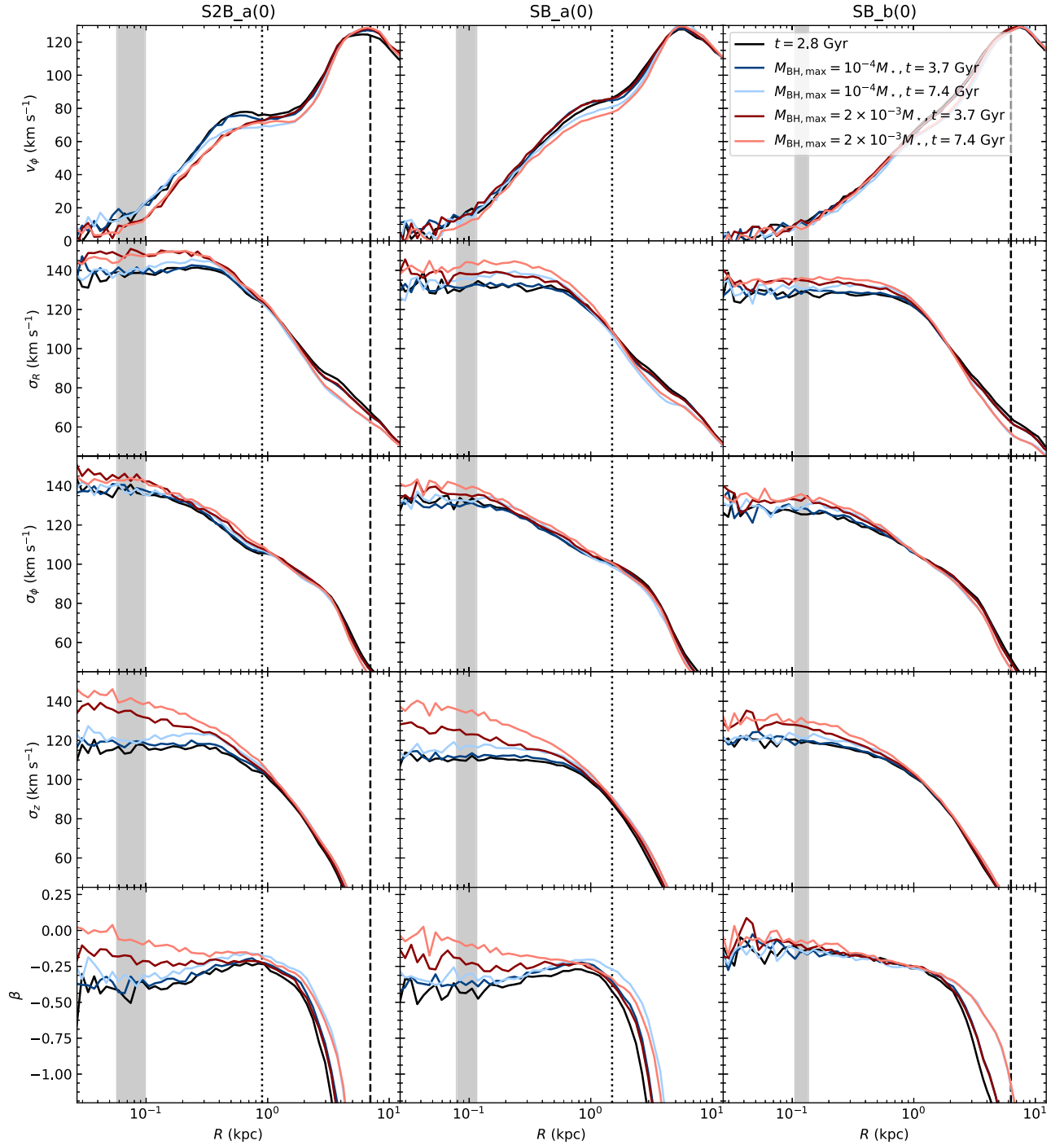


Figure 7. Similar to Figure 5, evolution of rotational velocity (v_ϕ), velocity dispersions (σ_R , σ_ϕ , σ_z), and anisotropy parameter [$\beta \equiv 1 - (\sigma_\phi^2 + \sigma_R^2)/2\sigma_z^2$], measured in annuli of equal radial interval in logarithmic space. The red and blue series of profiles represent the models with BHs of $M_{\text{BH,max}} = 2 \times 10^{-3} M_\star$ and $M_{\text{BH,max}} = 10^{-4} M_\star$, respectively. The gray region in each panel shows the range of the sphere-of-influence of the BH. The sizes of short bars and outer bars are marked with dotted and dashed vertical lines.

To summarize: the destruction of the short bar contributes to the growth of bulges. In this scenario, a massive and compact bulge forms by absorbing the stars of the short bar destroyed by BHs. A nuclear cusp forms, leading to a larger Sérsic index, although only $\sim 1\%$ – 2% of the total stellar mass is transferred inward from ~ 1 kpc. Du et al. (2017) argued that the growth of the BH can be mediated by the secular evolution of short bars. The present study shows that, in return, the BH regulates the growth of the bulge, the two acting as a self-regulated system.

4.3. Kinematics

The radial profiles of the cylindrical rotation velocity (v_ϕ) and the velocity dispersions (σ_R , σ_ϕ , σ_z) indicate that the models are dominated by random motion in their central region (Figure 7). The destruction of the short bar causes σ_z to increase sharply in the center of S2B_a and SB_a, while σ_ϕ and v_ϕ are only mildly affected. This may reflect the random scattering of bar orbits by the BH. The two-dimensional maps of σ_z

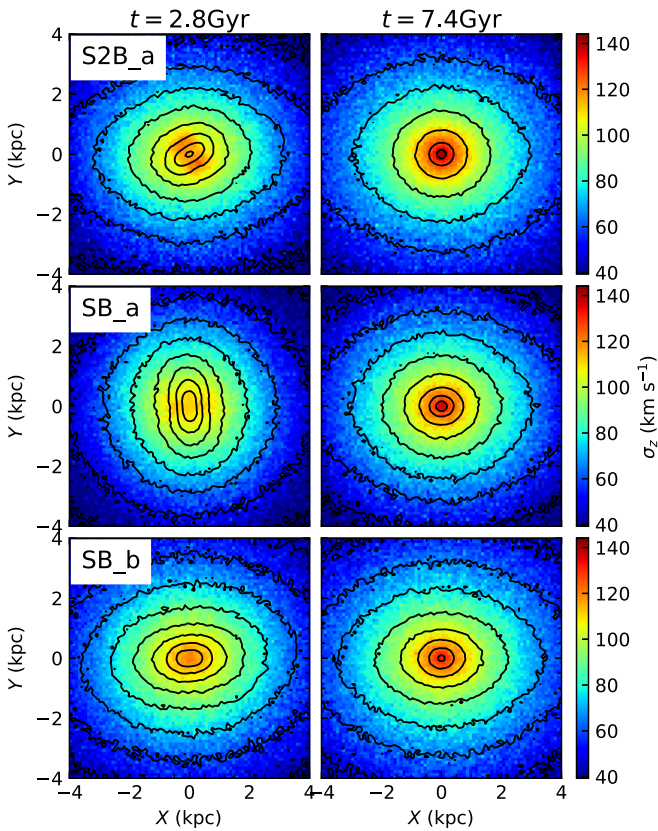


Figure 8. Evolution of the vertical velocity dispersion (σ_z), viewed face-on. The contours correspond to the distribution of surface density. At $t = 2.8$ Gyr, σ_z -humps (hollows) are perpendicular (parallel) to the short bars in both models S2B_a and SB_a.

(Figure 8) show that σ_z -humps/hollows⁵ (de Lorenzo-Cáceres et al. 2008; Du et al. 2016) disappear after the short bar is destroyed. The central peak in σ_z occurs at $t = 7.4$ Gyr, at which point the central region is also nearly isotropic, as judged by the anisotropic parameter, $\beta \equiv 1 - (\sigma_\phi^2 + \sigma_R^2)/2\sigma_z^2 \approx 0$ (Figure 7). Thus, a spheroidal structure dominated by random motions—a bulge—is created after the short bar is destroyed.

4.4. Evolution of the Bulges on Scaling Relations

Pseudo bulges are distinct from the classical bulge (reviewed by Kormendy & Kennicutt 2004). Classical bulges are thought to be spheroidal systems that form in violent, dissipative processes, such as gas-rich mergers (e.g., Toomre 1977; Aguerri et al. 2001), while pseudo bulges likely originate from slow internal processes (Kormendy et al. 2011). A widely accepted argument for advancing this theory is that classical bulges follow the same fundamental plane as elliptical galaxies (Kormendy et al. 2009, 2011; Fisher & Drory 2010), whereas pseudo bulges, including boxy/peanut bulges, are generally offset from this relation.

We examine our simulated bulges on the three scaling relations that have been commonly used to classify bulges (Figure 9), overlaid on the data adapted from Gadotti (2009). The observed bulges are classified according to the Kormendy (1977) relation of (Gadotti 2009, their Figure 8). The quantity

⁵ For details of σ -humps/hollows, see de Lorenzo-Cáceres et al. (2008; integral-field unit observations), Du et al. (2016; N -body simulations), and Du et al. (2017; theoretical interpretation).

$\langle \Sigma_e \rangle$ is the average stellar mass surface density within the half-mass-radius r_e , derived using the average surface luminosity and mass-to-light ratio from Gadotti (2009). We focus on the main group, as the bulges of the control group only evolve mildly at $t \geq 3.7$ Gyr. The simulation outputs for the two time steps are connected by a solid line. It is worth emphasizing that the absolute position of the model galaxies on the scaling relations are determined by an arbitrary scaling factor, and the most physically meaningful comparison is their relative evolution. The unfilled symbols indicate the results assuming a fiducial scaling of $M_* = 6 \times 10^{10} M_\odot$ and $h_R = 2.5$ kpc. To study the effect of unit scaling, we adjust the simulations to a reasonable mass range of $M_* = 2 \times 10^{10} - 2 \times 10^{11} M_\odot$. During the steady stage (Phase 3), the scale length of the disk is about $2.0 h_R$. The disk scale length in observations (Fathi et al. 2010) is ~ 5 kpc for galaxies in the same stellar mass range. We vary the length unit from 1.5 to 3 kpc, which covers the typical range of disk scale length for galaxies of this mass range. The results are shown by the shaded regions. At $t = 2.8$ Gyr (open triangles), the model bulges have diverse properties. All the bulges become more massive and compact at $t \geq 3.7$ Gyr (open circles), moving to the upper left of the $\langle \Sigma_e \rangle - r_e$ and $M_b - r_e$ diagrams. The bulge in model SB_b is relatively diffuse and less massive, thus falling among the pseudo bulge class. In comparison, at $t \geq 3.7$ Gyr the bulges in models S2B_a and SB_a are as massive and compact as observed classical bulges. The same trend holds for the relation between n and B/T . Therefore, the growth of bulges driven by the destruction of short bars may significantly blur the difference between pseudo and classical bulges. Some relatively less massive and compact classical bulges may form via secular evolution due to the destruction of short bars.

Figure 10 (left) shows the correlation between BH mass and bulge stellar mass, using as a comparison the data assembled in Kormendy & Ho (2013). The unfilled circles mark the results assuming the fiducial scaling for $t \geq 3.7$ Gyr, after the BH has grown. The dashed lines and the shaded regions are obtained by the same method used in Figure 9. Our simulations suggest that the mass ratio between BHs and bulges is constant at $M_{\text{BH}}/M_b \approx 0.006$ (red dashed line in the left panel). This is consistent with the median mass ratio observed in classical bulges. This constant M_{BH}/M_b results from the nearly constant bulge-to-total mass ratio ($M_b/M_* \approx 0.35$) obtained in the simulations and from our imposing a maximum BH mass allowed for secular processes, as suggested by Du et al. (2017). Model SB_b is clearly offset from the $M_{\text{BH}} - M_b$ relation because of the usage of the maximum BH mass. A galaxy hosting a single large-scale bar may not form BHs as massive as those in galaxies with short bars, and it may fall below the scaling relation of classical bulges and be more consistent with the pseudo bulges. Pseudo bulges may evolve toward the same scaling relation as classical bulges via the mechanism of short bar-mediated BH growth suggested in this study.

Similarly, Figure 10 (right) plots the $M_{\text{BH}} - \sigma_e$ relation, where σ_e is the average velocity dispersion of the bulge measured within r_e . The shaded band corresponds to varying the length unit between 1.5 and 3 kpc. The resulting slope of ~ 2 is clearly too shallow to match the observed slope of 4.4 (Kormendy & Ho 2013). However, our present very limited set of models cannot possibly be expected to produce a realistic match to the observations. They only suffice to demonstrate that our simulated bulges bear a close resemblance to classical bulges.

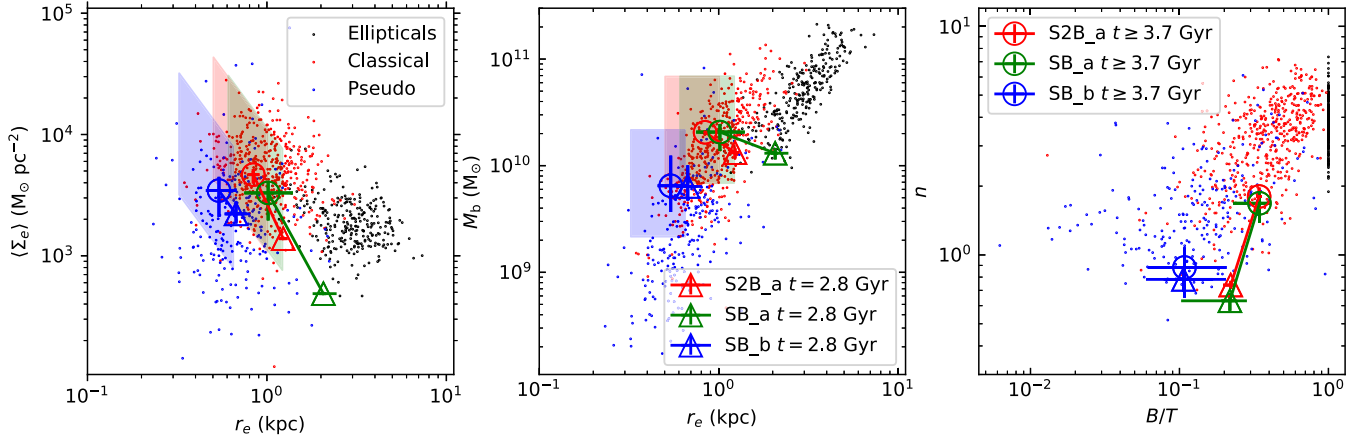


Figure 9. Scaling relations: (left) average surface mass density within the bulge effective radius $\langle \Sigma_e \rangle$ vs. the effective radius r_e ; (middle) bulge stellar mass M_b vs. r_e , and (right) Sérsic index n vs. bulge-to-total ratio B/T . The black, red, and blue points represent ellipticals, classical bulges, and pseudo bulges, respectively, adopted from Gadotti (2009). The results of our models are overlaid as open triangles (Phase 1, $t = 2.8$ Gyr) and circles (Phase 3, $t \geq 3.7$ Gyr) connected by solid lines. We average the results obtained from the decompositions using two bar functions and three inclination angles. Decomposition results from five snapshots of $t = 3.7$ – 7.4 Gyr are used for the cases of Phase 3. The error bars correspond to upper and lower limits. The shaded regions in the left and middle panels show the regions covered by reasonable scalings of the parameters of Phase 3 (see the text).

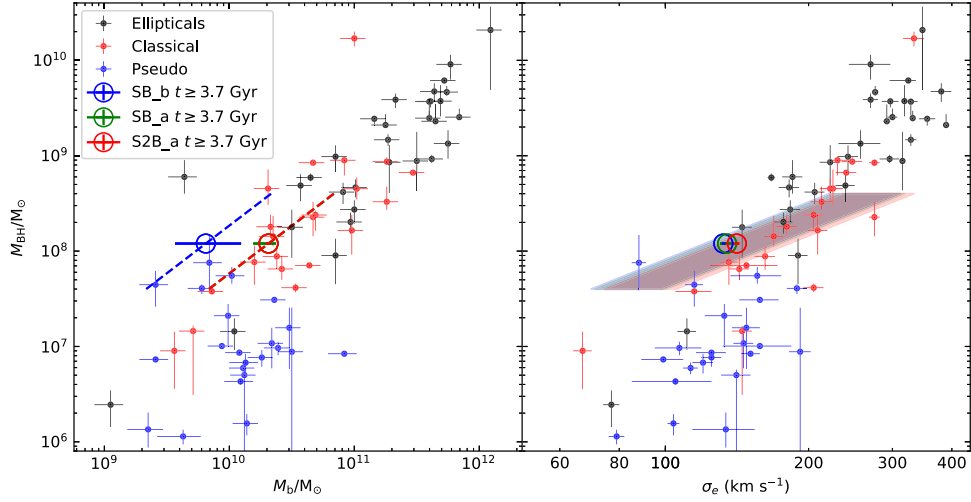


Figure 10. (Left) M_{BH} – M_b and (right) M_{BH} – σ_e relation of the models, where M_b is the bulge stellar mass and σ_e is the mean velocity dispersion within r_e . The parameters were obtained in the same manner as in Figure 9. The data for the ellipticals, as well as classical and pseudo bulges, are from Kormendy & Ho (2013). In the left panel, the mass ratio is constant along each dashed line. The red dashed line marks the constant mass ratio $M_{BH}/M_b \approx 0.006$. The shaded regions in the right panel show the reasonable scaling regions of the parameters (see the text). Note that in the left panel, SB_a (green circle) is almost completely covered by S2B_a (red circle).

We note that all three models have similar values of σ_e , and σ_e remains nearly the same during the growth of the BH, even though the bulge mass increases significantly and the bar structures evolve significantly. In our models σ_e may be largely determined by the total stellar mass of the system. In real galaxies or more realistic simulations, σ_e would be reduced by the formation of new stars, which is not implemented in our current treatment.

5. Discussion: A Channel of Forming Classical Bulges from Disks/Pseudo Bulges

We provide a potential evolutionary channel that allows disks to evolve into classical-like bulges without mergers. This scenario is illustrated in Figure 11. Du et al. (2015) showed that a short (inner) bar forms spontaneously when a dynamically cool, inner disk (gray circle in the top panel) exists. Such an inner disk may be built up gradually by gas

funneled inward due to perturbations from large-scale bars (Athanasoula 2005b) or tidal forces (Hernquist 1989). Short (inner) bars have been hypothesized to be an important mechanism for driving gas inflows on <100 pc scales, efficiently feeding BHs (e.g., Shlosman et al. 1989, second panel of Figure 11). Du et al. (2017) suggested that the maximum mass a BH can reach via secular evolution is about 0.1% of the total stellar mass, because a BH more massive than this threshold would destroy the inner bar. According to the result of this study, the remnants of short bars have properties similar to those of classical bulges. Therefore, an inner cold disk/bar can be transformed into a classical bulge under the influence of a BH. Classical bulges forming by this mechanism are likely to be younger and more metal-rich than typical classical bulges. It is interesting to note that classical bulges exhibit a clear bimodal distribution in age (Figure 9 of Gadotti 2009; see also Allen et al. 2006). Are the classical

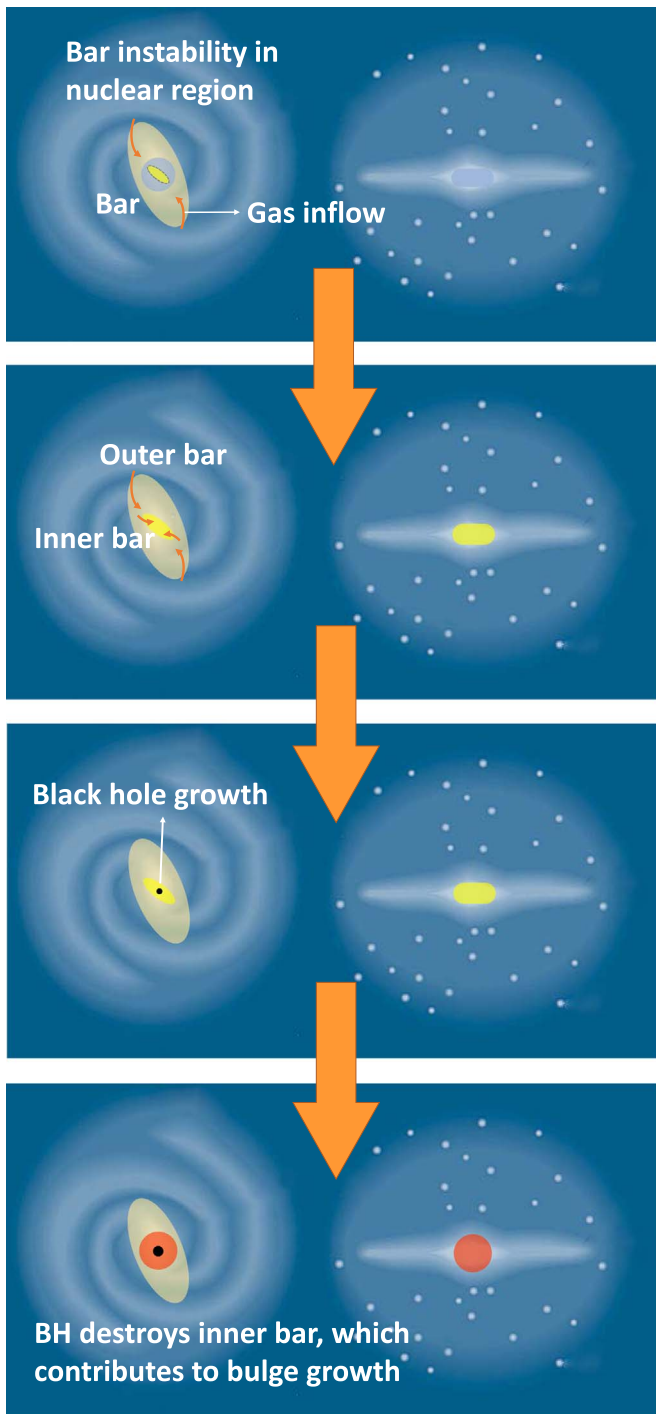


Figure 11. Schematic illustration of the scenario proposed in Section 5 on the coevolution between BHs and bulges due to the destruction of short bars.

bulges with young stellar populations formed from the destruction of short bars?

It is worth mentioning that the short bars invoked in our scenario need not be as stable and long-lived as those of our models. Many N -body+gas simulations generate gas-rich, short-lived nuclear bars (e.g., Friedli & Martinet 1993; Combes 1994; Shlosman & Heller 2002; Englmaier & Shlosman 2004; Wozniak 2015). Bulges may grow gradually by destroying recurring weak nuclear bars.

Scaling relations offer a useful, practical framework for constraining the formation and evolution of galaxies. While

classical and pseudo bulges occupy statistically different loci in the mean (e.g., on the Kormendy relation; see Gadotti 2009; Gao et al. 2019b), no clear boundary separates the two types. We propose that galaxies with inner short bars offer a channel for pseudo bulges to migrate into the territory of classical bulges. Classical bulges, therefore, may be a mixed bag; they are not all simply little ellipticals surrounded by disks. Breda & Papaderos (2018) also argue that secular processes in disks produce a continuum of bulge properties. The bulge formed by this new channel is not included in the bulge dichotomy proposed by Kormendy & Kennicutt (2004). Its moderate Sérsic index is likely to blur the difference between a real classical bulge and pseudo bulge. Because of this, the Sérsic index is not a clean discriminant between classical and pseudo bulges (Gao et al. 2019a).

6. Summary

Short ($\lesssim 1$ kpc) (inner) bars are an important mechanism for driving gas inflows to feed central BHs. Our previous work (Du et al. 2017) has shown that a BH of mass $\sim 0.1\%$ of the total stellar mass of the galaxy can destroy the inner bar, thereby self-limiting the growth of the BH. This paper examines in detail the consequences of this scenario for the central stellar distribution of the host galaxy. What is the fate of the remnant of the destroyed inner bar? We demonstrate that an initially boxy/peanut-shaped bulge with Sérsic index $n \lesssim 1$ gets transformed into a more massive, compact ($n \approx 2$), isotropic, slowly rotating spheroid that bears many of the characteristics of a classical bulge and in terms of their location on bulge scaling relations. We propose a new channel for forming classical bulges from the destruction of short bars formed from nuclear disks.

This work was supported by the National Science Foundation of China (11721303) and the National Key R&D Program of China (2016YFA0400702). We thank Peter Erwin for the constructive discussion. M.D. is supported by the grants “National Postdoctoral Program for Innovative Talents” (No. 8201400810) and “Postdoctoral Science Foundation of China” (No. 8201400927) from the China Postdoctoral Science Foundation. V.P.D. was supported by STFC Consolidated grant ST/R000786/1. V.P.D. acknowledges support from the Kavli Visiting Scholars Program for a visit to the KIAA during this work. We utilized the High-performance Computing Platform of Peking University.

ORCID iDs

Minghao Guo  <https://orcid.org/0000-0002-3680-5420>

Min Du  <https://orcid.org/0000-0001-9953-0359>

Luis C. Ho  <https://orcid.org/0000-0001-6947-5846>

Victor P. Debattista  <https://orcid.org/0000-0001-7902-0116>

Dongyao Zhao  <https://orcid.org/0000-0001-8592-7910>

References

- Aguerri, J. A. L., Balcells, M., & Peletier, R. F. 2001, *A&A*, 367, 428
 Allen, P. D., Driver, S. P., Graham, A. W., et al. 2006, *MNRAS*, 371, 2
 Athanassoula, E. 1992, *MNRAS*, 259, 328
 Athanassoula, E. 2005b, *MNRAS*, 358, 1477
 Athanassoula, E., Lambert, J. C., & Dehnen, W. 2005a, *MNRAS*, 363, 496
 Barnes, J. E., & Hernquist, L. 1996, *ApJ*, 471, 115
 Barth, A. J., Ho, L. C., Rutledge, R. E., & Sargent, W. L. W. 2004, *ApJ*, 607, 90

- Bell, E. F., Monachesi, A., Harmsen, B., et al. 2017, *ApJL*, 837, L8
- Bournaud, F., Duc, P. A., & Emsellem, E. 2008, *MNRAS*, 389, L8
- Breda, I., & Papaderos, P. 2018, *A&A*, 614, A48
- Cisternas, M., Jahnke, K., Inskip, K. J., et al. 2011, *ApJ*, 726, 57
- Clarke, A. J., Debattista, V. P., Nidever, D. L., et al. 2019, *MNRAS*, 484, 3476
- Combes, F. 1994, in *Mass-Transfer Induced Activity in Galaxies Conf. Univ. Kentucky*, ed. I. Shlosman (Cambridge: Cambridge Univ. Press), 170
- de Lorenzo-Cáceres, A., Falcón-Barroso, J., Vazdekis, A., & Martínez-Valpuesta, I. 2008, *ApJL*, 684, L83
- Debattista, V. P., Carollo, C. M., Mayer, L., & Moore, B. 2004, *ApJL*, 604, L93
- Debattista, V. P., Corsini, E. M., & Aguerri, J. A. L. 2002, *MNRAS*, 332, 65
- Debattista, V. P., Mayer, L., Carollo, C. M., et al. 2006, *ApJ*, 645, 209
- Debattista, V. P., & Shen, J. 2007, *ApJL*, 654, L127
- Dekel, A., Sari, R., & Ceverino, D. 2009, *ApJ*, 703, 785
- Du, M., Debattista, V. P., Shen, J., & Cappellari, M. 2016, *ApJ*, 828, 14
- Du, M., Debattista, V. P., Shen, J., Ho, L. C., & Erwin, P. 2017, *ApJL*, 844, L15
- Du, M., Shen, J., & Debattista, V. P. 2015, *ApJ*, 804, 139
- Du, M., Shen, J., Debattista, V. P., & de Lorenzo-Cáceres, A. 2017, *ApJ*, 836, 181
- Elmegreen, B. G., Bournaud, F., & Elmegreen, D. M. 2008, *ApJ*, 688, 67
- Elmegreen, B. G., & Elmegreen, D. M. 2005, *ApJ*, 627, 632
- Englmaier, P., & Shlosman, I. 2004, *ApJL*, 617, L115
- Erwin, P. 2004, *A&A*, 415, 941
- Erwin, P., & Sparke, L. S. 2002, *AJ*, 124, 65
- Fathi, K., Allen, M., Boch, T., Hatziminaoglou, E., & Peletier, R. F. 2010, *MNRAS*, 406, 1595
- Ferrarese, L., & Merritt, D. 2000, *ApJL*, 539, L9
- Filippenko, A. V., & Ho, L. C. 2003, *ApJL*, 588, L13
- Fisher, D. B., & Drory, N. 2008, *AJ*, 136, 773
- Fisher, D. B., & Drory, N. 2010, *ApJ*, 716, 942
- Friedli, D., & Martinet, L. 1993, *A&A*, 277, 27
- Gadotti, D. A. 2009, *MNRAS*, 393, 1531
- Gao, H., Ho, L. C., Barth, A. J., & Li, Z.-Y. 2019a, *ApJS*, submitted
- Gao, H., Ho, L. C., Barth, A. J., & Li, Z.-Y. 2019b, *ApJS*, 244, 34
- Gebhardt, K., Bender, R., Bower, G., et al. 2000, *ApJL*, 539, L13
- Genzel, R., Burkert, A., Bouché, N., et al. 2008, *ApJ*, 687, 59
- Gerhard, O. O., & Binney, J. 1985, *MNRAS*, 216, 467
- Greene, J. E., Ho, L. C., & Barth, A. J. 2008, *ApJ*, 688, 159
- Greene, J. E., Strader, J., & Ho, L. C. 2019, *ARA&A*, in press, arXiv:1911.09678
- Gültekin, K., Richstone, D. O., Gebhardt, K., et al. 2009, *ApJ*, 698, 198
- Håring, N., & Rix, H.-W. 2004, *ApJL*, 604, L89
- Hasan, H., & Norman, C. 1990, *ApJ*, 361, 69
- Hernquist, L. 1989, *Natur*, 340, 687
- Ho, L. C. 2008, *ARA&A*, 46, 475
- Hopkins, P. F., Cox, T. J., Younger, J. D., & Hernquist, L. 2009, *ApJ*, 691, 1168
- Hopkins, P. F., & Quataert, E. 2010, *MNRAS*, 407, 1529
- Hozumi, S. 2012, *PASJ*, 64, 5
- Inoue, S., & Saitoh, T. R. 2012, *MNRAS*, 422, 1902
- Jiang, Y.-F., Greene, J. E., Ho, L. C., Xiao, T., & Barth, A. J. 2011, *ApJ*, 742, 68
- Kim, M., Ho, L. C., Peng, C. Y., Barth, A. J., & Im, M. 2017, *ApJS*, 232, 21
- Kim, W.-T., Seo, W.-Y., & Kim, Y. 2012, *ApJ*, 758, 14
- Kormendy, J. 1977, *ApJ*, 218, 333
- Kormendy, J., Bender, R., & Cornell, M. 2011, *Natur*, 469, 374
- Kormendy, J., Fisher, D. B., Cornell, M. E., & Bender, R. 2009, *ApJS*, 182, 216
- Kormendy, J., & Ho, L. C. 2013, *ARA&A*, 51, 511
- Kormendy, J., & Kennicutt, R. C. 2004, *ARA&A*, 42, 603
- Laine, S., Shlosman, I., Knapen, J. H., & Peletier, R. F. 2002, *ApJ*, 567, 97
- Li, Z., Shen, J., & Kim, W.-T. 2015, *ApJ*, 806, 150
- Noguchi, M. 1998, *Natur*, 392, 253
- Noguchi, M. 1999, *ApJ*, 514, 77
- Okamoto, T. 2013, *MNRAS*, 428, 718
- Park, M.-J., Yi, S. K., Dubois, Y., et al. 2019, *ApJ*, 883, 25
- Peng, C. Y., Ho, L. C., Impey, C. D., & Rix, H.-W. 2002, *AJ*, 124, 266
- Peng, C. Y., Ho, L. C., Impey, C. D., & Rix, H.-W. 2010, *AJ*, 139, 2097
- Pfenniger, D., & Norman, C. 1990, *ApJ*, 363, 391
- Raha, N., Sellwood, J., James, R., & Kahn, F. 1991, *Natur*, 352, 411
- Reines, A. E., & Volonteri, M. 2015, *ApJ*, 813, 82
- Sales, L. V., Navarro, J. F., Theuns, T., et al. 2012, *MNRAS*, 423, 1544
- Scannapieco, C., White, S. D. M., Springel, V., & Tissera, P. B. 2009, *MNRAS*, 396, 696
- Sellwood, J. 2014, arXiv:1406.6606
- Shen, J., & Sellwood, J. A. 2004, *ApJ*, 604, 614
- Shlosman, I., Frank, J., & Begelman, M. C. 1989, *Natur*, 338, 45
- Shlosman, I., & Heller, C. H. 2002, *ApJ*, 565, 921
- Toomre, A. 1964, *ApJ*, 139, 1217
- Toomre, A. 1977, in *Evolution of Galaxies and Stellar Populations Proc. Conf. Yale Univ.*, ed. B. M. Tinsley, D. C. Larson, & R. B. Gehret (New Haven, CT: Yale Univ. Observatory), 401
- Tremaine, S., Gebhardt, K., Bender, R., et al. 2002, *ApJ*, 574, 740
- Vandenberg, D. A., Bolte, M., & Stetson, P. B. 1996, *ARA&A*, 34, 461
- Wang, L., Obreschkow, D., Lagos, C. d. P., et al. 2019, *MNRAS*, 482, 5477
- Wozniak, H. 2015, *A&A*, 575, A7
- Wu, Y.-T., Pfenniger, D., & Taam, R. E. 2016, *ApJ*, 830, 111
- Zhao, D., Ho, L. C., Zhao, Y., Shangguan, J., & Kim, M. 2019, *ApJ*, 877, 52
- Zolotov, A., Dekel, A., Mandelker, N., et al. 2015, *MNRAS*, 450, 2327